ISSN 1063-7788, Physics of Atomic Nuclei, 2017, Vol. 80, No. 5, pp. 919–927. © Pleiades Publishing, Ltd., 2017.
Original Russian Text © O.V. Bespalova, A.A. Klimochkina, 2017, published in Yadernaya Fizika, 2017, Vol. 80, No. 5, pp. 516–524.

NUCLEI
Theory

Calculation of Nucleon Densities in Calcium, Nickel, and Molybdenum Isotopes on the Basis of the Dispersive Optical Model

O. V. Bespalova* **and A. A. Klimochkina**

Skobeltsyn Institute of Nuclear Physics, Moscow State University, Moscow, 119991 Russia

Received March 9, 2017

Abstract—The radial distributions of proton and neutron densities in the even–even isotopes $^{40-70}$Ca and $^{48-78}$Ni and the analogous distributions of neutron densities in the even–even isotopes $^{92-138}$Mo were calculated on the basis of the mean-field model involving a dispersive optical potential. The respective root-mean-square radii and neutron-skin thicknesses were determined for the nuclei under study. In $N > 40$ calcium isotopes, the calculated neutron root-mean-square radius exhibits a fast growth with increasing N, and this is consistent with the prediction of the neutron-halo structure in calcium isotopes near the neutron drip line.

DOI: 10.1134/S1063778817050039

1. INTRODUCTION

The nuclear density is one of the fundamental quantities that characterize the structure of nuclei. In the case of stable nuclei, charge densities and charge root-mean-square radii were measured in electron-scattering experiments to a fairly high degree of precision. Neutron densities and root-mean-square radii were measured in reactions induced by strongly interacting particles, such as protons and alpha particles, and in experiments that studied nuclear effects in exotic atoms. The uncertainties in those experiments were an order of magnitude larger than those in the case of protons. The development of techniques for producing and accelerating beams of radioactive nuclei opened the possibility of studying a new region of nuclei—those remote from the beta-stability valley—and put to the fore nuclear-physics branches associated with studying them. In the past few decades, unexpected properties have been discovered in precisely these nuclei. Among other things, we would like to mention here the existence of a skin and neutron and proton halos, as well as the disappearance of traditional magic numbers and the emergence of new ones.

Investigation of the structure of unstable medium-mass and heavy nuclei is of importance for the development of neutron-star physics [1]. However, experimental data on the distribution of nucleons in such nuclei are scanty. In calcium isotopes lying near the neutron drip line, the relativistic continuum Hartree–Fock model [2] and the nonrelativistic Hartree–Fock–Bogolyubov model [3] predict a neutron-halo structure. According to the relativistic Hartree–Bogolyubov model [4], a neutron-halo structure is also formed in zirconium isotopes near the neutron drip line.

The dispersive optical model (DOM) [5] makes it possible to calculate single-particle properties of unstable nuclei via a physically validated extrapolation of the parameters of this model to the region of such nuclei [6]. In the present study, the distributions of the proton (charge) and neutron densities in calcium and nickel isotopes and of the neutron density in molybdenum isotopes are calculated on the basis of the mean-field model involving a dispersive optical potential (DOP). In addition, the ability of the dispersive optical model to predict the formation of a neutron-halo structure in calcium isotopes near the neutron drip line (predictive power of the model) is explored.

2. FUNDAMENTALS OF THE MODEL

In the dispersive optical model [5], the mean field is complex-valued, its locally equivalent real, $V(r,E)$, and imaginary, $W_I(r,E)$, parts being related by a dispersive equation; that is,

$$V(r,E) = V_{\rm HF}(r,E) + \frac{P}{\pi}\int\limits_{-\infty}^{\infty} W_I(r,E')\left(\frac{1}{(E'-E)} - \frac{1}{(E'-E_{\rm F})}\right)dE'. \quad (1)$$

Thus, one represents the real part of the dispersive optical potential as the sum of a component $V_{\rm HF}(r,E)$ that belongs to the Hartree–Fock type and which

*E-mail: besp@sinp.msu.ru

changes smoothly with energy and a dispersive component $\Delta V(r,E)$, which depends sharply on E in the vicinity of the Fermi energy $E_{\rm F}$. The surface, $\Delta V_d(r,E)$, and volume, $\Delta V_s(r,E)$, parts of the dispersive component take effectively into account nucleon correlations that are, respectively, concentrated at the surface and distributed over the volume. The fundamentals of the model used in the present study were outlined in [6].

The nucleon single-particle energies, E_{nlj}, and wave functions, $\Phi_{nlj}(\mathbf{r})$, were calculated by employing the iteration method to solve the Schrödinger equation

$$\left[\frac{-\nabla^2}{2m}+V(r,E_{nlj})\right]\Phi_{nlj}(\mathbf{r})=E_{nlj}\Phi_{nlj}(\mathbf{r}), \quad (2)$$

where $V(r,E_{nlj})$ is the real part of the dispersive optical potential and has the form

$$-V(r,E_{nlj})=V_{\rm HF}(r,E_{nlj})+\Delta V_s(r,E_{nlj}) + \Delta V_d(r,E_{nlj})+U_{so}(r,E_{nlj})-V_C(r). \quad (3)$$

The radial dependence of the components $V_{\rm HF}$ and $\Delta V_{s(d)}$ was specified by the Woods–Saxon function and its derivative. The single-particle wave functions, which are solutions of the Schrödinger equation, can be represented as the product of the real and angular components; that is,

$$\Phi_{nlj}(\mathbf{r})=\frac{u_{nlj}(r)}{r}Y_{lm}(\Omega). \quad (4)$$

In calculating quantities that characterize the single-particle motion of a nucleon in the nucleus being considered, the effect of a nonlocal character of the dispersive optical potential was taken into account via the wave function

$$\bar{u}_{nlj}(r)=C_{nlj}P_{nlj}(r)u_{nlj}(r), \quad (5)$$

where the Perey factor $P_{nlj}(r)$ is given by

$$P_{nlj}(r)=\left[1-\frac{d}{dE}V_{\rm HF}(r,E)\right]^{1/2} \quad (6)$$

and the normalization factor C_{nlj} was found from the condition

$$\int\limits_0^\infty \bar{u}^2_{nlj}(r)dr^3=1. \quad (7)$$

In just the same way as in [7], the proton and neutron matter densities were calculated within the single-particle approach on the basis of the expression

$$\rho_{p(n)}(r)=\frac{1}{4\pi}\sum_{nlj}(2j+1)N_{nlj}\bar{u}^2_{nlj}(r). \quad (8)$$

A transition from the proton density to the charge density was performed via employing the relation

$$\rho_{\rm ch}(r)=(\pi a^2)^{-3/2}\int\rho_p(r')\exp\left[-(r-r')^2/a^2\right]d\mathbf{r}', \quad (9)$$

where $a^2=0.4\,{\rm fm}^2$ takes approximately into account the proton charge form factor and the center-of-mass motion for the nucleus being considered.

Within the dispersive optical model, one determines the occupation probabilities for single-particle states, N_{nlj}, according to approximate expressions. In particular, we employ the expression

$$N_{nlj}=1-\int\limits_0^\infty \bar{u}^2_{nlj}(r)\left[\{m^*_{\rm HF}(r,E_{nlj})/m\}^{-1}\right. \quad (10)$$
$$\left.\times\pi^{-1}\int\limits_{E_{\rm F}}^\infty\frac{W_I(r,E')}{(E'-E_{nlj})^2}dE'\right]dr, E_{nlj}<E_{\rm F},$$

$$N_{nlj}=\int\limits_0^\infty \bar{u}^2_{nlj}(r)\left[\{m^*_{\rm HF}(r,E_{nlj})/m\}^{-1}\right.$$
$$\left.\times\pi^{-1}\int\limits_{-\infty}^{E_F}\frac{W_I(r,E')}{(E'-E_{nlj})^2}dE'\right]dr, E_{nlj}>E_{\rm F},$$

where $m^*_{\rm HF}$ is the effective Hartree–Fock mass; that is,

$$m^*_{\rm HF}(r,E)/m=1-\frac{d}{dE}V_{\rm HF}(r,E). \quad (11)$$

Their use frequently leads to underestimated values of the total number of neutrons (protons), $N_{n(p)}=\sum_{nlj}(2j+1)N_{nlj}$, in bound nuclear states with respect to the number $N(Z)$. This underestimation may stem from strong short-range correlations dominated by tensor forces in the proton–neutron interaction [8], which shift the components of the spectral function [5] toward positive energies by several hundred MeV units [9]. In order to determine the parameter $V_{\rm HF}(E_{\rm F})$ by fitting the calculated number of nucleons, $N_{n(p)}$, to the number $N(Z)$ for the nucleus being considered, we therefore used the values N_{nlj} determined by the BCS formula

$$N_{nlj}(E_{nlj}) = 1/2\left(1-\frac{(E_{nlj}-E_{\rm F})}{\sqrt{(E_{nlj}-E_{\rm F})^2+(\Delta)^2}}\right). \quad (12)$$

We took the energies calculated with a dispersive optical potential for the energies E_{nlj} and employed, for the gap parameter, its empirical value

$$\Delta=-1/4\{S_i(A+1)-2S_i(A)+S_i(A-1)\}, \quad (13)$$

Table 1. Root-mean-square charge radii $\langle r_{\rm ch}\rangle$ (in fm units) of stable calcium and nickel isotopes

Nucleus	Experiment [20–22]	DOM
^{40}Ca	3.4777(12)	3.47
^{42}Ca	3.5086(13)	3.52
^{44}Ca	3.5182(13)	3.52
^{46}Ca	3.4956(13)	3.52
^{48}Ca	3.4772(13)	3.48
^{58}Ni	3.7757(13)	3.84
^{60}Ni	3.8110(13)	3.84
^{62}Ni	3.8386(14)	3.85
^{64}Ni	3.8553(14)	3.86

$$i = n, p,$$

which was found from data on the nucleon separation energies $S_{n(p)}$ [10–12].

The spectroscopic factors and root-mean-square radii of single-particle states were calculated by the formulas

$$S_{nlj} = \int\limits_0^\infty \bar{u}^2_{nlj}(r)\,[\bar{m}(r, E_{nlj})/m]^{-1}\,dr, \qquad (14)$$

$$R^{\rm rms}_{nlj} = \left[\int\limits_0^\infty \bar{u}^2_{nlj}(r) r^4 dr\right]^{1/2}. \qquad (15)$$

In Eq. (14), $\bar{m}(r, E_{nlj})/m$ is the ratio of the effective energy-dependent mass to the total nucleon mass:

$$\bar{m}(r, E)/m = 1 - [m/m^*_{\rm HF}(r, E)]\,\frac{d}{dE}V(r, E). \quad (16)$$

The spatial sizes of a nucleus were characterized by the root-mean-square radius $\langle r_{{\rm ch},p,n}\rangle$,

$$\langle r_{{\rm ch},p,n}\rangle = \left[\frac{\int\limits_0^\infty r^4 \rho_{{\rm ch},p,n}(r)dr}{\int\limits_0^\infty r^2 \rho_{{\rm ch},p,n}(r)dr}\right]^{1/2}, \qquad (17)$$

where $\rho_{{\rm ch},p,n}$ stands for, respectively, the charge (ch), proton (p), and neutron (n) density.

3. DENSITY DISTRIBUTIONS OF STABLE CALCIUM AND NICKEL ISOTOPES

The nuclear spectroscopy of stable calcium and nickel isotopes was studied in [13–15]. In the present study, the radial density distributions $\rho_{{\rm ch},p,n}$ and the radii $\langle r_{{\rm ch},p,n}\rangle$ for the even–even isotopes $^{40-48}$Ca and $^{48-64}$Ni were calculated along with ρ_n and $\langle r_n\rangle$ for the isotopes $^{92-100}$Mo by employing the DOP parameters found earlier. The DOP parameters for the stable isotopes $^{40-48}$Ca and $^{58-64}$Ni were determined in [13, 14, 16] from an analysis of the most precise and reliable information about the proton and neutron energies and occupation probabilities for single-particle orbits near the Fermi energy $E_{\rm F}$. This information was obtained by the joint evaluation of the data on nucleon-stripping and nucleon-pickup reactions on the same nucleus. Some parameters were fixed according to the global parameters from [17] of the traditional optical model by employing the procedure for constructing dispersive optical potentials from [6]. The parameters of the neutron dispersive optical potential for molybdenum isotopes were also determined in [6].

By way of example, Fig. 1 shows the calculated density distributions $\rho_{\rm ch}$ in the isotopes ^{40}Ca and ^{64}Ni. We performed the respective calculations at the values found for the proton DOP parameters in [14] for the ^{40}Ca nucleus and in [16] for the isotopes ^{58,60,62}Ni, employing the occupation probabilities N_{nlj} in the form (10) and (12), respectively. This figure shows that the results of the calculations are in good agreement with experimental data from [18, 19]. The distribution ρ_n calculated for the ^{92}Mo nucleus is presented in Section 4.

The charge radii $\langle r_{\rm ch}\rangle$ for stable calcium and nickel isotopes are given in Table 1. The results of the calculations agree well with the experimental values $\left\langle r^{\rm expt}_{\rm ch}\right\rangle$ for calcium isotopes from [20, 21] and the experimental values for nickel isotopes from [22]. The deviation takes the largest value of 1.5% for the isotope ^{58}Ni. The experimental and calculated charge radii $\langle r_{\rm ch}\rangle$ in nickel isotopes grow with increasing N in the isotopes. It is noteworthy that the calculated radii $\langle r_{\rm ch}\rangle$ grow more slowly than the experimental values $\left\langle r^{\rm expt}_{\rm ch}\right\rangle$ do. The above agreement can be improved via varying the DOP parameters (in particular, the parameter $r_{\rm HF}$) in calculating $\langle r_{\rm ch}\rangle$. The change in the radius $\left\langle r^{\rm expt}_{\rm ch}\right\rangle$ in response to an increase in the number of neutrons in stable calcium isotopes does not reduce to a smooth growth because of the doubly magic nature of the isotopes ^{40,48}Ca. The effect exerted by the filling of the $1f_{7/2}$ shell with neutrons on

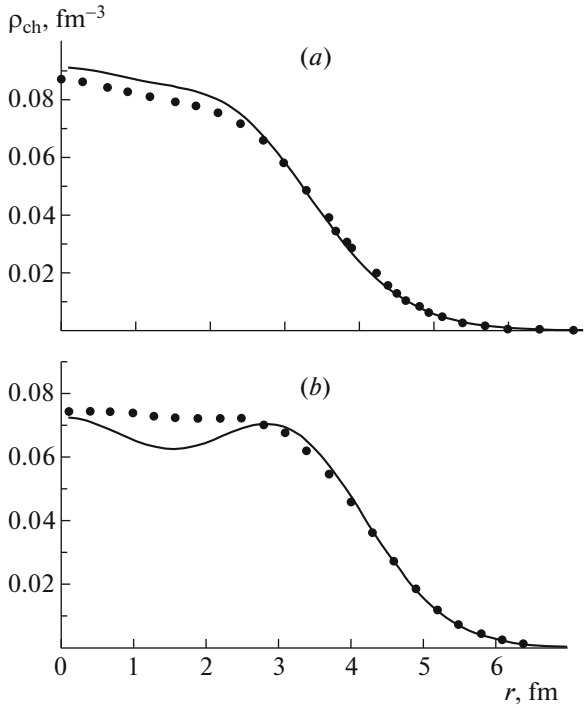

Fig. 1. Charge density distributions $\rho_{\rm ch}$ in the (a) ^{40}Ca and (b) ^{64}Ni nuclei: (points) experimental data from [18, 19] and (curves) results of the calculations with a dispersive optical potential.

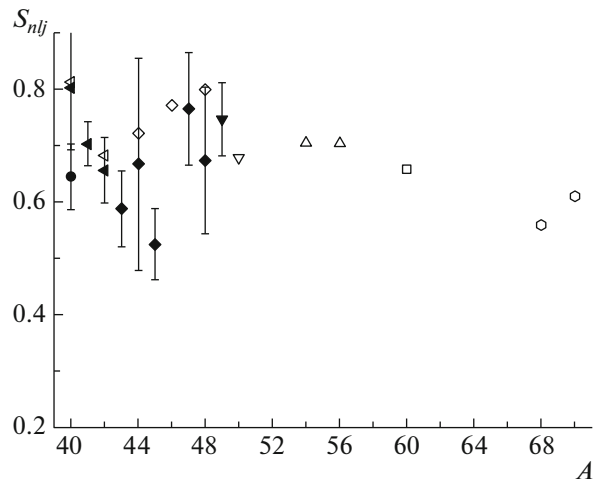

Fig. 2. Spectroscopic factors S_{nlj} for the following neutron single-particle states in calcium isotopes according to (closed symbols) experimental data from [25, 26] and (open symbols) the results of DOP calculations: (closed and open left-oriented triangles) $1d_{3/2}$, (closed and open diamonds) $1f_{7/2}$, (closed and open down-oriented triangles) $2p_{3/2}$, (open up-oriented triangles) $2p_{1/2}$, (open boxes) $1f_{5/2}$, (open circles) $1g_{9/2}$.

the charge radii $\left\langle r_{\rm ch}^{\rm expt}\right\rangle$ in the isotopes $^{40-48}$Ca was discussed in [23]. In the present study, the dynamics of the change in $\left\langle r_{\rm ch}^{\rm expt}\right\rangle$ could be described owing to the inclusion of shell effects [24], which consist in the decrease in the imaginary part of the dispersive optical potential near the Fermi energy $E_{\rm F}$ for nuclei in which $N\,(Z)$ is a magic number in comparison with what we have for neighboring nuclei.

The spectroscopic factors S_{nlj} calculated according to Eq. (14) for valence neutron states are given in Fig. 2. The experimental values $S_{nlj}^{\rm expt}$ for neutron states of stable calcium isotopes in the vicinity of $E_{\rm F}$ were obtained in [25, 26] from an analysis of data on (d,p), $(p,\,d)$, and $(e,e'p)$ reactions. The factors S_{nlj} calculated for stable isotopes reflect the magic properties of the numbers $N=20$ and 28. For example, the $S_{1d_{3/2}}$ and $S_{1f_{7/2}}$ reach maximum values in the cases of ^{40}Ca and ^{48}Ca, respectively. The fact that the results of DOP calculations agree with experimental data on the single-particle properties of stable nuclei gives sufficient grounds to employ this approach to predict theoretically density distributions in unstable nuclei.

4. DENSITY DISTRIBUTIONS OF UNSTABLE CALCIUM, NICKEL, AND MOLYBDENUM ISOTOPES

A procedure for performing a physically validated extrapolation of the DOP parameters from the region of stable nuclei to the region of unstable nuclei, for which experimental information about nucleon scattering on them and about their single-particle properties is limited or is absent was proposed in [6]. This procedure makes use of the predictions based on the systematics of global parameters [17] within the traditional (nondispersive) optical model and leads to agreement between the total number of nucleons, N_n (N_p), and the number $N(Z)$ for the nucleus being considered.

For the unstable calcium, nickel, and molybdenum isotopes studied here, the dispersive optical potential was determined in [6, 24]. The imaginary part of the neutron dispersive optical potential for calcium isotopes near the neutron drip line was corrected in the present study. In [24], the parameter d_3 in the energy dependence of the surface absorption $W_d(E)$ for the isotope ^{70}Ca was determined by requiring that the energy E_- of the last predominantly occupied state and the energy E_+ of the first predominantly free state be close to, respectively, the sign-reversed neutron-separation energies $-S_n(^{70}{\rm Ca})$ and $-S_n(^{71}{\rm Ca})$ [10]. This condition corresponds to the idea that $N=50$ is a "strong" magic number. In the vicinity of the nucleon drip line, it is natural to expect the weakening of shell effects in accordance with the calculations

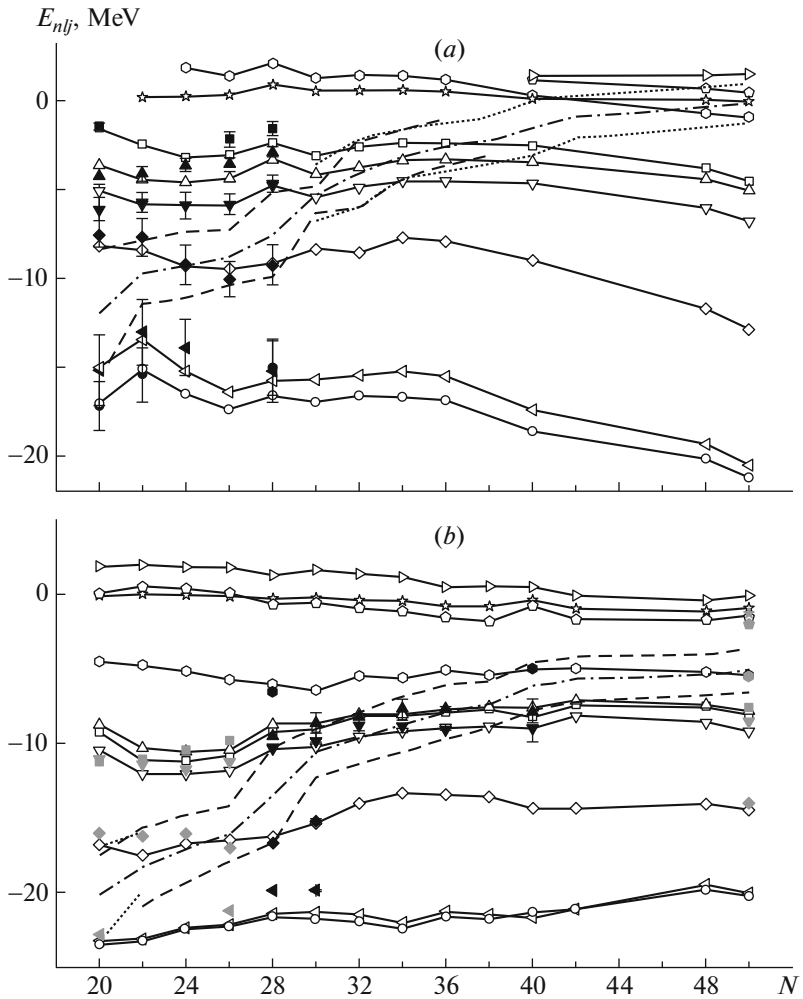

Fig. 3. Neutron single-particle energies E_{nlj} of the following states in the even–even (a) calcium and (b) nickel isotopes according to (symbols shaded in black) experimental data, (symbols shaded in gray) estimations, and (open symbols) the results of DOP calculations: (closed and open circles) $2s_{1/2}$, (black, gray, and open left-oriented triangles) $1d_{3/2}$, (black, gray, and open diamonds) $1f_{7/2}$, (black, gray, and open down-oriented triangles) $2p_{3/2}$, (black and open triangles) $2p_{1/2}$, (black, gray, and open boxes) $1f_{5/2}$, (gray and open hexagons) $1g_{9/2}$, (gray and open stars) $3s_{1/2}$, (gray and open pentagons) $2d_{5/2}$, and (open right-oriented triangles) $2d_{3/2}$. The dashed and dotted curves stand for the energies $-S_n(N,Z)$ and $-S_n(N+1,Z)$ according to [10] and [11], respectively; the dash-dotted curve represents the Fermi energy $E_{\rm F}$; and the solid curves correspond to the DOP calculations.

performed in [27] on the basis of the Hartree–Fock–Bogolyubov model with SkP Skyrme forces. Available data on scattering and single-particle properties of bound states of stable nuclei were analyzed in [28] on the basis of the dispersive optical model. This analysis revealed that, for $N > Z$ nuclei, the $(N - Z)/A$ dependence of W_d is weaker for neutrons than for protons. In [29], it was assumed that W_d for neutrons is independent of $(N - Z)/A$. It turned out that this made it possible to match the spectroscopic factors calculated for states of calcium isotopes in the vicinity of the Fermi energy with experimental data. We have performed model-dependent calculations with two versions of the surface absorption W_d for calcium isotopes in the vicinity of the neutron drip line. In the first version, the absorption W_d was independent of $(N - Z)/A$, its parameters being chosen to be equal to the global parameters for ^{40}Ca [17]. In the second version, we fixed all of the parameters at the values obtained in [17]; this was not so only for the parameter d_3 (for the results of the respective calculation, see Fig. 3a), which was set to 8.0 MeV for the isotopes ^{60,68,70}Ca—that is, reduced in relation to $d_3 = 11.5$ MeV [17]. In either version, we set the geometric parameters $r_{\rm HF}$ and $a_{\rm HF}$ to, respectively, r_V and a_V [17] and took the spin–orbit potential from [17] as well. The parameter values of $V_{\rm HF}(E_{\rm F}) = 46.1$, 44.6, and 44.5 MeV were found for the isotopes ^{60,68,70}Ca, respectively, by fitting the calculated number N_n to the number N for the isotope

being considered. In determining N_n for the isotopes ^{60,68,70}Ca, the respective sum included the $3s_{1/2}$ and $2d_{5/2}$ states, which lie above the Fermi energy. These states play an important role in the formation of the neutron-halo structure in calcium isotopes near the neutron drip line [2, 3]. The above two versions of the calculation led to close values of the energies E_{nlj} near the Fermi energy E_{F}.

The evolution of single-particle neutron spectra in the calcium isotopes (DOP parameter set featuring $d_3 = 8$ MeV) and in the $N \leqslant 50$ nickel isotopes is illustrated in Figs. 3*a* and 3*b*, respectively. The experimental and estimated energies E_{nlj} for unstable nickel isotopes were obtained in [30, 15]. The neutron single-particle spectrum of molybdenum isotopes was calculated on the basis of the dispersive optical model, and the results of those calculations were presented in [6]. According to calculations involving a dispersive optical potential, the particle–hole energy gap G in the isotope ^{70}Ca is about 0.8 MeV. This value is substantially smaller than the G value in the stable $N = 50$ isotones. In particular, we have $G \approx 4$ MeV for ^{92}Mo (see [6]). This result agrees with the idea that shell effects become weaker as the isotopes being considered approach the neutron drip line [27]. According to the mass-model prediction from [11], about 20 neutrons separate the ^{78}Ni nucleus from the neutron drip line. From Fig. 3*b*, one can see that the calculation on the basis of the dispersive optical model suggests that $N = 50$ is a magic number of neutrons for the ^{78}Ni nucleus. By way of example, we indicate that the energy $-S_n$ (^{78}Ni) is close to the energy E_{nlj} of the $1g_{9/2}$ state, while the energy $-S_n$ (^{79}Ni) is close to the energy of the $2d_{5/2}$ state. Figure 4*a*, which gives the gap G for the $N = 50$ isotones ^{92}Mo, ^{78}Ni, and ^{70}Ca, shows that it decreases as one approaches the neutron drip line. The evolution of the proton single-particle spectra of calcium and nickel isotopes is shown in Figs. 5*a* and 5*b*, respectively. It corresponds to the idea that the numbers $Z = 20$ and 28 have magic properties. From Fig. 5, one can see that the energies $-S_p(N, Z)$ and $-S_p(N, Z+1)$ are close to the energies E_- and E_+, respectively.

The neutron root-mean-square radii $\langle r_n \rangle$ in calcium, nickel, and molybdenum isotopes are shown in Fig. 6 versus the relative neutron excess $(N - Z)/A$. One can see that the calculated radius of the ^{70}Ca nucleus, $\langle r_n \rangle = 4.80$ fm, exceeds substantially the value that arises for this nucleus upon the linear extrapolation of the dependence $\langle r_n\,((N - Z)/A)\rangle$ for the $N \leqslant 40$ isotopes. A sharp growth of $\langle r_n \rangle$ was predicted on the basis of the relativistic continuum Hartree–Fock model in [2] and on the basis of the nonrelativistic Hartree–Fock–Bogolyubov model in [3]. The conclusion that a giant neutron halo (featuring more than two neutrons) may be formed in the isotope ^{70}Ca was drawn in those studies. Figure 4*b* illustrates the growth of the calculated radius $\langle r_n \rangle$ in the $N = 50$ isotones ^{92}Mo, ^{78}Ni, and ^{70}Ca with increasing $(N - Z)/A$.

In the ^{70}Ca nucleus, halo neutrons are in states of energy above the Fermi energy, which, in this nucleus, is close to zero ($E_{\mathrm{F}} = -0.175$ MeV [11]). According to the calculation with a dispersive optical potential, one of these states, $3s_{1/2}$, is still bound, its radius ($R^{\mathrm{rms}}_{nlj} = 12.0$ fm) being more than twice as long as the radius ($R^{\mathrm{rms}}_{nlj} = 4.9$ fm) of the lower lying $1g_{9/2}$ state (see Table 2). Further, $2d$ states already lie at positive energies, their radius R^{rms} exceeding 9 fm. The occupation probability N_{nlj} (10) for the $3s_{1/2}$ state is 0.44, and 0.9 of a nucleon populates it. In the $2d_{5/2}$ and $2d_{3/2}$ states, whose occupation probabilities are $N_{nlj} = 0.25$ and 0.1, respectively, there are 1.5 nucleons and 0.3 of a nucleon, respectively. It is noteworthy that the radii R^{rms} of states up to the $1g_{9/2}$ state are close in the $N = 50$ isotones ^{92}Mo, ^{78}Ni, and ^{70}Ca; in contrast, the radii of the $3s_{1/2}$ and $2d$ states grow substantially upon going over from the stable isotope ^{92}Mo to the isotope ^{70}Ca, which lies in the vicinity of the neutron drip line. The neutron density distributions calculated for these isotones with the dispersive optical potential constructed in the present study are given in Fig. 7. The surface layer is substantially more extended in the ^{70}Ca nucleus than in the ^{78}Ni and ^{92}Mo nuclei.

The $N = 86$ isotope ^{138}Mo lies near the neutron drip line, its Fermi energy being $E_{\mathrm{F}} = -0.09$ MeV

Table 2. Root-mean-square radii R^{rms}_{nlj} (in fm units) of neutron single-particle states near the Fermi energy E_{F} in $N = 50$ isotones according to calculations with a dispersive optical potential

Subshell	^{92}Mo	^{78}Ni	^{70}Ca
$2d_{3/2}$	5.47	7.46	9.83
$2d_{5/2}$	5.22	6.08	9.05
$3s_{1/2}$	5.62	7.67	12.0
$1g_{9/2}$	4.71	4.83	4.90
$1f_{5/2}$	4.28	4.57	4.51
$2p_{1/2}$	4.42	4.80	4.99
$2p_{3/2}$	4.32	4.64	4.75

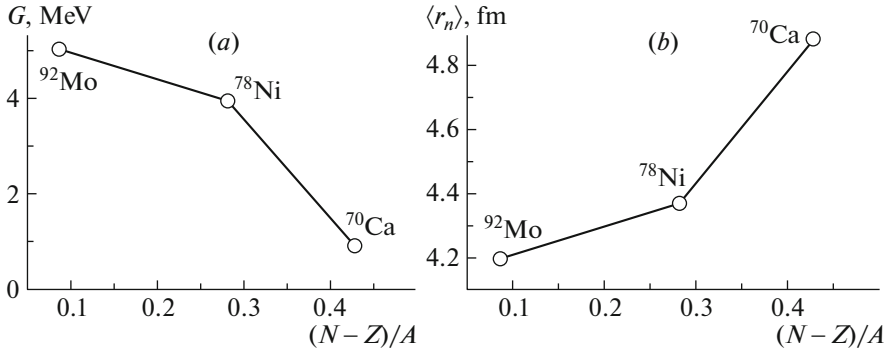

Fig. 4. (a) Particle-hole gap G and (b) neutron root-mean-square radius $\langle r_n \rangle$ for the $N = 50$ isotones ^{92}Mo, ^{78}Ni, and ^{70}Ca. The solid curves on display represent the results of the calculations performed with a dispersive optical potential.

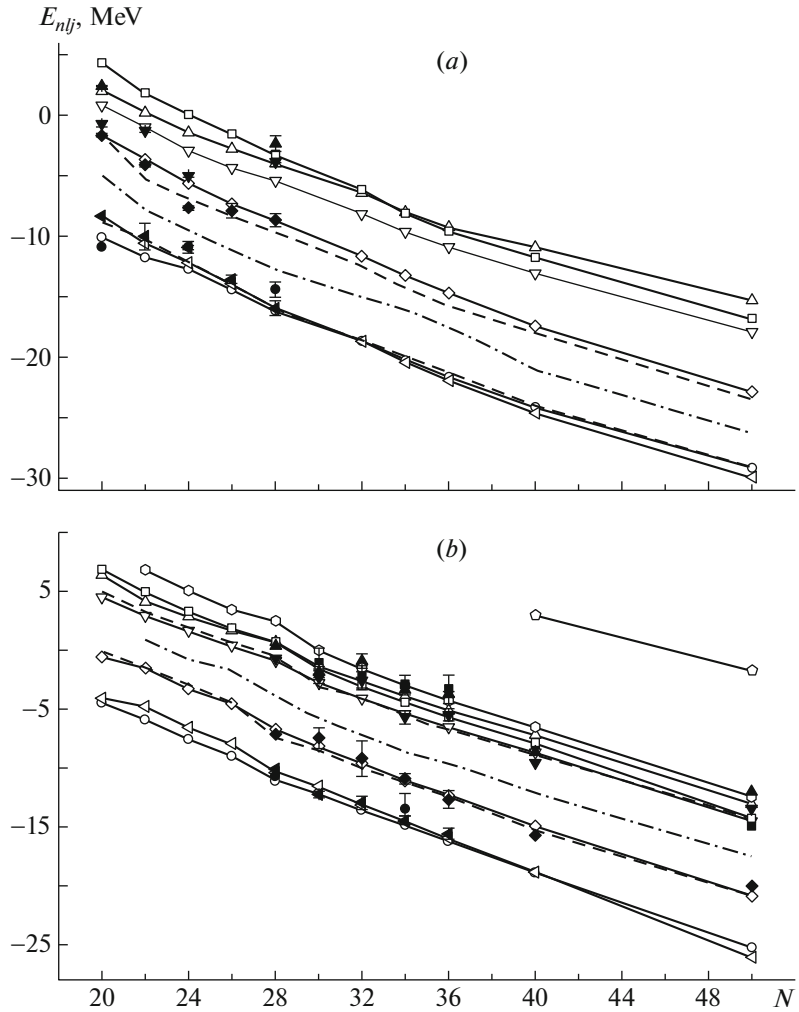

Fig. 5. Proton single-particle energies E_{nlj} in even–even (a) calcium and (b) nickel isotopes. The notation for the points is identical to that in Fig. 3. The dashed lines represent the energies $-S_p(N, Z)$ and $-S_p(N, Z+1)$ according to [11]. The solid curves correspond to a calculation with a dispersive optical potential. The dashed-dotted line stands for the Fermi energy.

[12]. According to the calculation with the dispersive optical potential constructed in the present study, the $3p_{1/2}$ and $3p_{3/2}$ neutron states in this nucleus have the radii of $R^{\rm rms}_{nlj} = 10.4$ and 9.4 fm, respectively, which exceed substantially the radii of the neighboring states—for example, the radius of

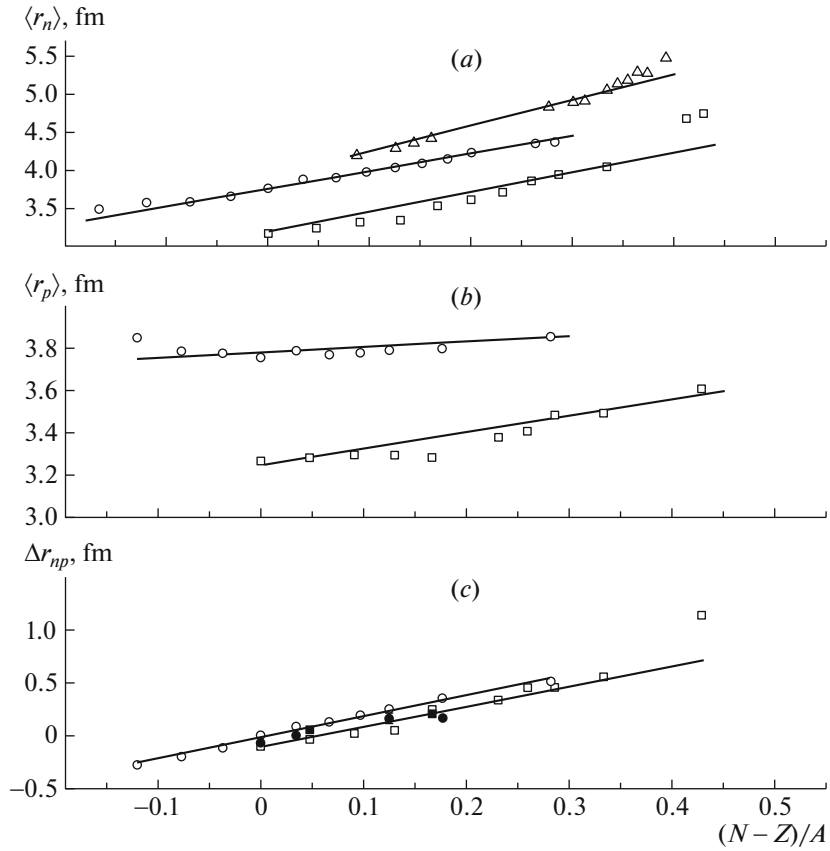

Fig. 6. (*a*) Neutron root-mean-square radii $\langle r_n \rangle$ in calcium, nickel, and molybdenum isotopes versus the relative neutron excess, (*b*) proton root-mean-square radii $\langle r_p \rangle$ in calcium and nickel isotopes, and (*c*) neutron-skin thickness Δr_{np} in calcium and nickel isotopes according to (closed symbols) experimental data from [31, 32] and (open symbols) results of calculations with a dispersive optical potential: (closed and open boxes) calcium, (closed and open circles) nickel isotopes, and (open triangles) molybdenum isotopes. The solid curves on display were calculated with a dispersive optical potential.

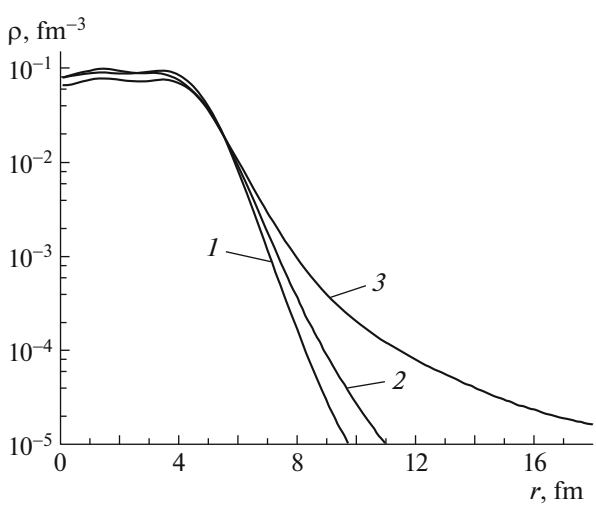

Fig. 7. Neutron density distributions according to the results of the calculations performed within the single-particle approach with a dispersive optical potential for the isotopes (curve *1*) ^{92}Mo, (curve *2*) ^{78}Ni, and (curve *3*) ^{70}Ca.

$R^{\rm rms}_{nlj} = 6.8$ fm for the lower lying $2f_{7/2}$ state and the radius of 6.2 fm for the higher lying $1h_{9/2}$ state. For the isotope in question, this leads to the radius $\langle r_n \rangle$ larger than that which the linear extrapolation of the dependence $\langle r_n\,((N-Z)/A)\rangle$ for $N \leqslant 80$ yields (see Fig. 6*a*). In accordance with the occupation probabilities N_{nlj} given by expression (10), there are 3.5 neutrons in $3p$ states of the ^{138}Mo nucleus. This result complies with the predictions of the Hartree–Fock–Bogolyubov method for the formation of the neutron-halo structure in the neighboring $124 \leqslant N \leqslant 138$ zirconium isotopes [31].

For calcium isotopes and $20 \leqslant N \leqslant 50$ nickel isotopes, the proton radius $\langle r_{\rm p} \rangle$ and neutron-skin thickness $\Delta r_{np} = \langle r_n \rangle - \langle r_p \rangle$ calculated with the aforementioned dispersive optical potential are presented in Figs. 6*b* and 6*c*, respectively. The calculated values of Δr_{np} are compared with the experimental data, $\Delta r^{\rm expt}_{np}$, obtained for ^{40,42,48}Ca and ^{58,64,68}Ni in [32, 33] and compiled in [34, 35]. The thickness Δr_{np} calculated for the isotope ^{70}Ca exceeds substantially the

value to which the dependences $\Delta r_{np}((N-Z)/A)$ determined for calcium and nickel isotopes that lie far from the neutron drip line tend.

In accordance with the shell effect, the spectroscopic factor $S_{1g_{9/2}}$ is also greater in ^{70}Ca than in ^{68}Ca (see Fig. 2), but it does not reach values in excess of 0.8, which are characteristic of stable isotopes. Once again, this result can be associated with the weakening of the shell effect near the nucleon drip line.

5. CONCLUSIONS

Special features of the spatial neutron-density and proton-density (charge-density) distributions in $20 \leqslant N \leqslant 50$ calcium and nickel isotopes and the neutron-density distribution in $50 \leqslant N \leqslant 96$ molybdenum isotopes have been studied on the basis of the mean-field model involving a dispersive optical potential. Good agreement with experimental data on charge-density distributions and root-mean-square radii has been attained for stable calcium and nickel isotopes.

As one approaches the neutron drip line, the calculated neutron particle–hole energy gap G corresponding to the number of $N = 50$ decreases, which demonstrates the weakening of the shell effect. According to the calculation with the dispersive optical potential constructed in the present study, the isotope ^{70}Ca, which lies in the vicinity of the neutron drip line, features a neutron halo containing more than two nucleons and has a root-mean-square radius $\langle r_n \rangle$ that significantly exceeds the radius of halo-free $N = 50$ isotones. For molybdenum isotopes, the calculated radius $\langle r_n \rangle$ also exhibits a sharp growth as they approach the neutron drip line. This agrees with the results of the calculations performed in [31] with the aim of exploring the possible formation of the halo structure in neighboring zirconium isotopes lying near the neutron drip line.

ACKNOWLEDGMENTS

This work was supported by Russian Foundation for Basic Research (project no. 16-32-00388 mol_a).

REFERENCES

1. M. Baldo and G. F. Burgio, Rep. Prog. Phys. **75**, 026301 (2012).
2. J. Meng, H. Toki, J. Y. Zeng, et al., Phys. Rev. C **65**, 041302 (R) (2002).
3. J. Terasaki, S. Q. Zhang, S. G. Zhou, and J. Meng, Phys. Rev. C **74**, 054318 (2006).
4. J. Meng and P. Ring, Phys. Rev. Lett. **80**, 460 (1998).
5. C. Mahaux and R. Sartor, Adv. Nucl. Phys. **20**, 1 (1991).
6. O. V. Bespalova, A. A. Klimochkina, and T. I. Spasskaya, Phys. At. Nucl. **79**, 586 (2016).
7. M. Jaminon, C. Mahaux, and H. Ngô, Nucl. Phys. A **440**, 228 (1985).
8. R. Subedi et al., Science **320**, 1476 (2008).
9. W. H. Dickhoff and C. Barbieri, Prog. Part. Nucl. Phys. **52**, 377 (2004).
10. M. Wang, G. Audi, A. H. Wapstra, et al., Chin. Phys. C **36**, 1603 (2012).
11. H. Koura, T. Tachibana, M. Uno, and M. Yamada, Prog. Theor. Phys. **113**, 305 (2005).
12. S. Goriely, N. Chamel, and J. M. Pearson, Phys. Rev. C **82**, 035804 (2010).
13. O. V. Bespalova, I. N. Boboshin, V. V. Varlamov, T. A. Ermakova, B. S. Ishkhanov, E.A. Romanovsky, T. I. Spasskaya, and T. P. Timokhina, Phys. At. Nucl. **68**, 191 (2005).
14. O. V. Bespalova, I. N. Boboshin, V. V. Varlamov, B. S. Ishkhanov, E. A. Romanovsky, and T. I. Spasskaya, Phys. At. Nucl. **66**, 644 (2003).
15. O. V. Bespalova, I. N. Boboshin, V. V. Varlamov, T. A. Ermakova, B. S. Ishkhanov, A. A. Klimochkina, S. Yu. Komarov, H. Koura, E. A. Romanovsky, and T. I. Spasskaya, Phys. At. Nucl. **74**, 1521 (2011).
16. O. V. Bespalova, T. A. Ermakova, A. A. Klimochkina, E. A. Romanovsky, and T. I. Spasskaya, Phys. At. Nucl. **78**, 873 (2015).
17. A. J. Koning and J. P. Delaroche, Nucl. Phys. A **713**, 231 (2003).
18. H. J. Emrich, PhD Thesis (Univ. of Mainz, 1983).
19. G. Beuscher, PhD Thesis (Univ. of Mainz, 1983).
20. C. W. P. Palmer, P. E. G. Baird, S. A. Blundell, et al., J. Phys. B **17**, 2197 (1984).
21. H. D. Wohlfahrt, E. B. Shera, M. V. Hoehn, et al., Phys. Rev. C **23**, 533 (1981).
22. A. Steudel, U. Triebe, and D. Wendlandt, Z. Phys. A **296**, 189 (1980).
23. B. S. Ishkhanov, M. E. Stepanov, and T. Yu. Tretyakova, Moscow Univ. Phys. Bull. **69**, 1 (2014).
24. O. V. Bespalova, E. A. Romanovsky, and T. I. Spasskaya, Phys. At. Nucl. **78**, 118 (2015).
25. J. Lee, J. A. Tostevin, B. A. Brown, et al., Phys. Rev. C **73**, 044608 (2006).
26. G. J. Kramer, H. P. Blok, and L. Lapikás, Nucl. Phys. A **679**, 267 (2001).
27. J. Dobaczewski et al., Phys. Rev. C **53**, 2809 (1996).
28. J. M. Mueller, R. J. Charity, R. Shane, et al., Phys. Rev. C **83**, 064605 (2011).
29. R. J. Charity, J. M. Mueller, L. G. Sobotka, and W. H. Dickhoff, Phys. Rev. C **76**, 044314 (2007).
30. H. Grawe and M. Lewitowicz, Nucl. Phys. A **693**, 116 (2001).
31. Y. Zhang, M. Matsuo, and J. Meng, Phys. Rev. C **86**, 054318 (2012).
32. C. J. Horowitz et al., Phys. Rev. C **85**, 032501(R) (2012).
33. D. M. Rossi et al., Phys. Rev. Lett. **111**, 242503 (2013).
34. C. J. Batty, E. Friedman, H. J. Gils, and H. Rebel, Adv. Nucl. Phys. **19**, 1 (1989).
35. B. A. Brown, S. E. Massen, and P. E. Hodgson, J. Phys. G **5**, 1655 (1979).